Available online at www.sciencedirect.com
ScienceDirect
Astroparticle Physics 29 (2008) 104–116
Astroparticle Physics
www.elsevier.com/locate/astropart

Single photon counting approach for imaging atmospheric Cherenkov telescopes

O. Catalano *, M.C. Maccarone, B. Sacco

Istituto di Astrofisica Spaziale e Fisica Cosmica di Palermo, Istituto Nazionale di Astrofisica, Via Ugo La Malfa 153, 90146 Palermo, Italy[1]

Received 16 May 2007; received in revised form 29 November 2007; accepted 29 November 2007
Available online 9 January 2008

Abstract

The aim of this article is to present a single photon counting technique applied to the imaging atmospheric Cherenkov telescopes as an alternative to the charge integration technique used by most experiments in the field. A comparison of the two techniques has been performed, assuming suitable and realistic telescope layouts but different methods to treat and convert the electrical signals at the output of the light sensors. A set of γ-ray induced showers, with primary energies ranging from 300 GeV to 10 TeV, has been simulated for this comparison. The study has been performed both for a single telescope and for a three-telescope array. The results show, in both cases, considerably higher trigger efficiencies in the single photon counting method, with respect to the analog one, particularly at the lowest energies. Single telescope energy thresholds for the two methods are also reported and discussed.

PACS: 95; 95.55.Ka; 95.85.Pw

Keywords: Imaging atmosphere Cherenkov telescopes; γ-Ray astronomy; Extensive air showers; Detection techniques; Single photon counting mode

1. Introduction

The imaging atmospheric Cherenkov (IAC) technique is an advanced and successful method to detect extensive air showers (EAS) by measuring the Cherenkov light produced by primary photons/particles crossing the Earth atmosphere [1,2]. This technique opened a window to the ground-based γ-ray astronomy in the very high energy (VHE) range (from 50 GeV up to more than 10 TeV) and is still continuously improving detection performance and sensitivity. Nowadays, after the pioneering work of Whipple [3] and HEGRA [4], a variety of experiments are operating and produce important and exciting results (CANGAROO-III [5], VERITAS [6], MAGIC [7], H.E.S.S. [8]).

Basically, an imaging atmospheric Cherenkov telescope consists of an optical system with few degrees field of view (FoV $\leqslant 5°$) and of a multi-pixel camera placed at its focus. In order to achieve a good sensitivity at the lowest energies and accurate estimation of nature, direction and energy of the primary, the collecting area of the optical system has to be of the order of many tens of square meters and the pixel size of the camera must be around 0.2°. A configuration with more than one telescope is actually preferable: the stereoscopic approach strongly improves the general performance (angular and energy resolution, hadrons discrimination, core location resolution) and minimizes the rate of events triggered by the diffuse night sky background (NSB) light and single muons; furthermore, a larger detection area is achievable.

Many authors [9] have emphasised the importance of using fast photon sensors and fast electronics to disentangle the Cherenkov light, which is produced coherently in space and time (of the order of 10 ns), from the incoherent but significantly fluctuating NSB light. The photon sensors currently used are photomultipliers (PMTs); they guarantee a fast response (of the order of 2 ns) to incoming

* Corresponding author.
E-mail address: Osvaldo.Catalano@iasf-palermo.inaf.it (O. Catalano).
[1] http://www.iasf-palermo.inaf.it.

0927-6505/$ - see front matter © 2007 Elsevier B.V. All rights reserved.
doi:10.1016/j.astropartphys.2007.11.011

photons, good gain, quantum efficiency of about 20%, low intrinsic noise (dark current), easy assembling and maintenance. Front end, read-out and trigger electronics shape and amplify the analog pulses from the light sensors in the focal plane, digitalize them for the read out and data buffering, and perform the trigger decision.

Considerable efforts were made in the past to improve the sensitivity at the lowest energies, mainly designing systems with increased optical collection area, higher focal plane pixelization and use of several telescopes. Not many attempts have considered the possibility of a different approach regarding the conversion of light into electrical signals and their processing. In this paper we develop the basic concept and the implementation of an approach based on the *Digital* single photon counting (SPC) method as alternative to the *Analog* charge collection method currently used in imaging atmospheric Cherenkov experiments. The comparison of performance between these two types of signal processing will allow to establish, preliminarily, benefits and limits of the proposed approach and, consequently, to assess the technical feasibility and costing. As detailed below, the comparison is made for realistic and comparable telescope layouts, obviously changing the signal collection and processing method.

This paper is organized as follows: Section 2 describes the various assumptions used in the comparison; the simulation chain is described in Section 3; the results are detailed in Section 4, followed by a discussion and conclusions in Section 5. The crosscheck between experimental data and pulse simulation is given in Appendix.

2. Working assumptions

In order to simplify the comparison and the interpretation of the results, let us consider two identical hypothetical arrays labeled **A** (using Analog mode) and **D** (using Digital mode). The geometry of the **A** and **D** arrays is kept identical, as well as the basic structure of each telescope: the optical system and the PMT detectors are exactly the same, and consequently the total detection efficiencies are equal. The main difference existing between **A** and **D** is obviously the way the electrical signals from the anodes of the PMTs are treated: in **A** the charge is collected, and in **D** the signal photons are counted. Moreover, while for configuration **A** we have chosen a pixel size matching what is currently used in most IAC experiments, in configuration **D** pixels with half that size were considered. The smaller pixel size for configuration **D** is necessary to minimize the photon pile-up probability per pixel which limits the SPC method. With current telescopes this is about 20% at 1 TeV. A breakdown of the working assumptions, together with the related set-up values, is given below.

2.1. Telescopes array geometry

Three identical imaging Cherenkov telescopes, posed at the vertexes of an isosceles triangle (80 m height, 80 m basis) form the array considered in this study, as sketched in Fig. 1.

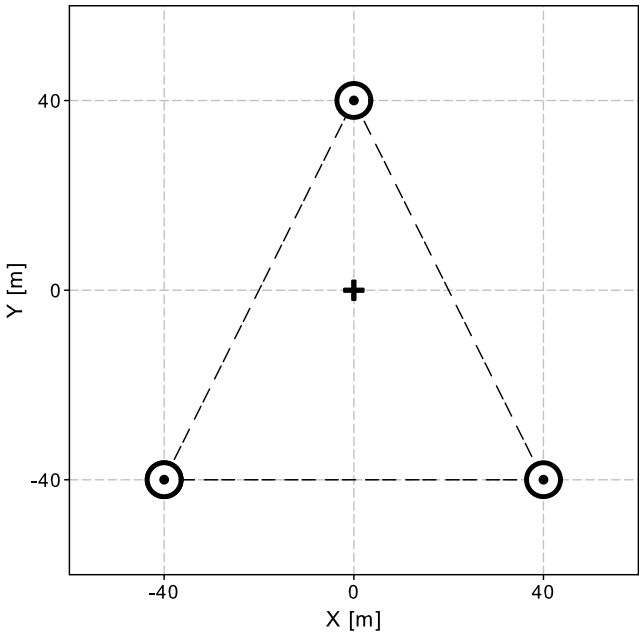

Fig. 1. Schematic view of the hypothetical array.

2.2. Optics

The telescopes have the f-number = 1.2 and 3.5 m^2 collecting area. The optics considered in the simulations refers to the H.E.S.S. optics [8] with the point spread function (PSF) as given in Fig. 2.

2.3. Focal plane

The focal plane is formed by 10×10 multi-anode photomultipliers (MAPMT), Hamamatsu R7600-03-M64 [10], covering a FoV of 6.4×6.4 square degrees. Each

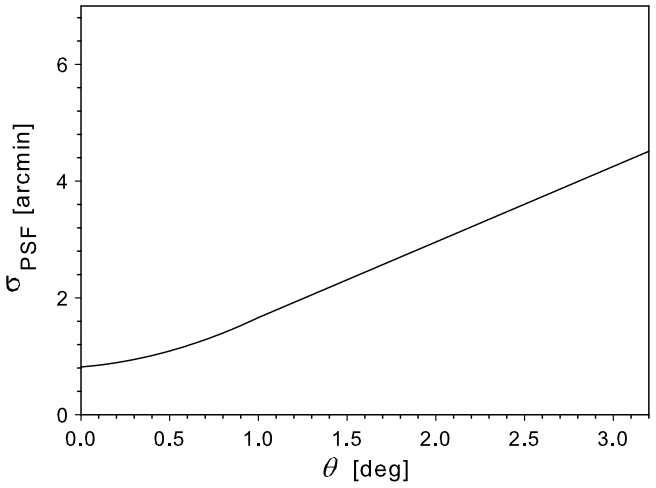

Fig. 2. Point spread function: standard deviation vs. the angular distance from the optical axis.

MAPMT, coupled with light guides, has a matrix of 8×8 pixels with a resulting pixel dimension of 3.25 mm corresponding to 0.08° subtended angle for the **D** configuration. In array **A**, the pixels are grouped 2×2, so resulting in 6.5 mm and 0.16° subtended angle. A total of 6400 pixels results for **D**, and 1600 pixels for **A**. The number of PMTs remains unchanged for both the configurations and they are supposed to operate at negative high voltage and same gain.

2.4. Front-end and trigger electronics

Front-end and trigger electronics are the elements that mainly distinguish the two configurations. A concise description of the electronics and related functions in each of the two hypothetical arrays follows.

2.4.1. *A* configuration

The pixel front-end electronics is organized as a chain made of an inverting 1 GHz preamplifier, a shaping filter and a 1 GHz to 10 bits FADC (fast analog-to-digital converter). This electronics chain allows the conversion of the electrical pulse (accumulated charge) to ADC counts. The relative measurement provided by ADC counts is then converted to equivalent *pe*s (photo-electrons) knowing the mean charge produced by a single *pe*. The mean *pe* charge can be statistically measured with the SER (single electron response) technique. Finally each pixel, sampled every GTU (gate time unit), 10 ns wide, is recorded in a cycle memory with the relevant position, relative time and equivalent *pe* number. Trigger logics is implemented on sectors of 8×8 pixels, with sector overlap of 4 pixels pitch in the left, right and diagonal directions, corresponding to 81 equivalent sectors. A trigger is generated when a required number of pixels has signals above a defined threshold.

2.4.2. *D* configuration

The pixel front-end electronics is constituted by an inverting 1 GHz preamplifier, a discriminator, and a pulse former. To reproduce faithfully the anode-pixel pulses, a high-speed linear inverting preamplifier is directly connected to each anode. An adjustable threshold discriminator shapes the amplified pulse to a standard digital logic level. This signal is sampled every GTU of 10 ns and ready to be recorded. At any GTU the map of the 64 pixels of all the MAPMTs containing the digitalized pulses in binary form is recorded into a cycle memory, one for each MAPMT, of appropriate depth. The discriminator is fast enough to disentangle double hits with a resolution of less than 10 ns. Trigger logic assures the suppression of accidental coincidences due to the NSB diffuse light; this logic is implemented on sectors of 16×16 pixels and with sector overlap of 8 pixels pitch in the left, right and diagonal directions, corresponding to 81 equivalent sectors. A trigger is generated when a more than a certain number of pixels has a signal.

3. The simulation chain

In order to study the response, in terms of trigger efficiency, for the two specified approaches, detailed simulations were needed. A set of simulated gamma showers at fixed energy was produced and the Cherenkov light was processed through the optical system to the camera in the focal plane; a signal pulse simulation module was then developed, as well as an *ad hoc* Monte Carlo simulation code for the estimation of NSB for the **A** and **D** configurations. When dealing with real instruments, accidental triggers due to NSB require special attention: setting a realistic telescope trigger threshold avoids the potential blindness of the detector caused by an excessive dead time. Once the operating trigger thresholds for the two configurations have been obtained, simulated showers were processed by a further simulation module incorporating the trigger algorithms described in Section 2 and with the calculated trigger threshold as input. Such a simulation chain allowed us to provide results in terms of trigger efficiency for a single telescope and for a 3-fold coincidence telescopes array for both the **A** and **D** configurations.

3.1. Air showers

The CORSIKA simulation code [11] has been used to generate the Cherenkov light, at level of single photons, from gamma induced air showers detected at 2150 m asl; the effects of the atmosphere and a set of detector parameters values were included; in particular: atmosphere transparency, optics PSF and efficiency and MAPMT quantum efficiency as a function of the Cherenkov photon wavelength, and a constant reduction factor to take into account light guide transparency and photomultiplier collecting efficiency.

The CORSIKA code (version 6.5, with QGSJET [12,13] as high-energy hadronic interaction model) was applied using its option CERARY so to obtain a set of physics simulation data common to both the **A** and **D** configurations, leaving to a further step (see Section 3.2) the inclusion of the parameters specific of each configuration. Furthermore, to increase the sample statistics, we moved each array along a number of randomly chosen positions within a square of 800 m side length. In CORSIKA, this corresponds to moving the shower core location with respect to the center of the array; and we can use a same shower many times during the trigger and analysis phase.

A consistent set of vertical gamma-induced showers has been simulated, for a total of 220,000 showers at 0.3 TeV, and 20,000 at each of the remaining primary energies: 0.5, 1, 2, 5 and 10 TeV. The CORSIKA simulated gamma-induced showers were further enriched by Poissonian NSB noise uniformly distributed in the camera pixels.

3.2. Pixel signal

Depending on the mode of operation, the signal pulse simulation is clearly different. For the single photon count-

ing mode, the setting of the discriminator threshold is sufficient to determine the counting efficiency, irrespective of the number of *pe*s forming the pulse (the counting efficiency is close to 95%, see Appendix) whereas, for the analog mode, the measurement of the single *pe* mean charge is required.

Pulse generation is, however, a common step to both the configurations. Taking into account the nominal characteristics of the R7600 MAPMT (gain, anode pulse rise time, transit time spread, dark count and noise factor), the signal pulse has been simulated according to the photomultiplier equivalent circuit equation (as response to a fast exponential decay transient stimulus with time constant τ_s):

$$V_o(t) = \frac{G \cdot N \cdot e_c \cdot R}{\tau - \tau_s} \cdot \left[e^{-\frac{t}{\tau_s}} - e^{-\frac{t}{\tau}} \right] \quad (1)$$

where $V_o(t)$ is the output signal in Volt, G is the gain, N refers to the number of photoelectrons, e_c is the elementary charge, and $\tau = RC$ is the output circuit time constant. The relative variance of the anode pulse (effect of dynodes multiplication noise) has been statistically introduced, as described in Appendix. In addition, white noise (electronics noise) has been incorporated to complete the pulse generation simulation.

It is good practice to study the single electron response (SER), i.e. the response to a single primary electron for a given photomultiplier. The SER depends on the characteristics of the photomultiplier used and measures the capability to resolve a single *pe*. Moreover, the characteristic differential pulse height spectrum allows to extract the required information on the mean *pe* charge, $\overline{Q}_{pe}$, expressed as:

$$\overline{Q}_{pe} = \frac{q \cdot \sum_{i=1}^{n} Ch_i \cdot N_i}{\sum_{i=1}^{n} N_i} \quad (2)$$

with q corresponding to the channel charge resolution, Ch_i $(i = 1, \ldots, n)$ the ADC channels, and N_i $(i = 1, \ldots, n)$ the associated counts of the ith channel. Without entering in the details of the simulation and SER measurement technique (see Appendix for more details), we show in Fig. 3 the SER simulated output and, for comparison, the SER as measured in the laboratory [14] for a pixel of the considered MAPMT, after dark current subtraction. As shown in Fig. 3, the simulated spectrum reproduces faithfully the measured one, leading to a difference less than 5% between the mean charge values.

The sampling of the anode signal with the FADC (1 GHz to 10 bits) is then performed and the resulting number of equivalent *pe*s is obtained by means of a conversion factor making use of the mean charge as found by SER analysis. Fig. 4 summarizes the simulation steps involved in the pixel pulse conversion from analog to digital. Using the superposition principle, single *pe*s arriving at the pixel with their own relative times (from CORSIKA simulation) are converted in voltage pulses, inverted and summed; estimated electronics noise is also added at this stage. The summed signal is then shaped and sampled by the FADC.

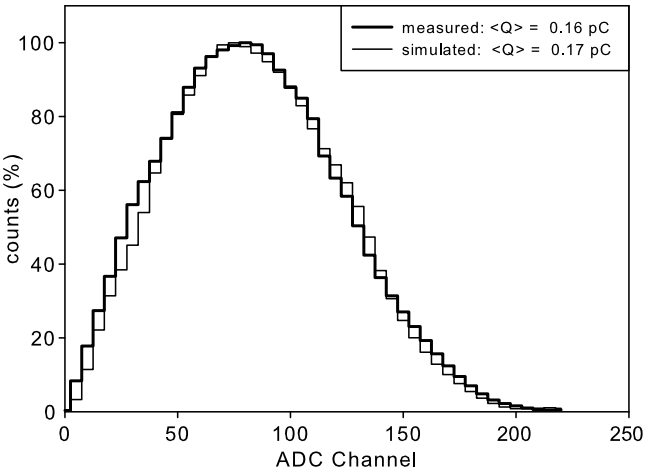

Fig. 3. Comparison of the simulated and measured single electron response spectra.

The value of equivalent *pe*s, obtained by summing up the FADC bins and dividing the total sum by the number of ADC counts per *pe*, is then recorded.

For each pixel in the focal plane we assume gain uniformity among all the anodes[2] ($\sim$30% measured value), no cross-talk between adjacent pixels ($\sim$4% measured value), and no afterpulses ($\sim$2% measured value). In the case of **A**, the grouping of 2×2 channels (as indicated in Section 2.3) is performed to obtain larger pixels than in the **D** camera.

3.3. Night sky background

The night sky background (NSB) and its intrinsic fluctuations are a considerable source of noise. Poisson fluctuations of the NSB light cause undesired accidental coincidences that have to be accounted for in order to optimize the trigger threshold. As described in Section 2, the telescope trigger of both the **A** and **D** configurations is based on fast pattern recognition of overlapping sectors with selection criteria specific to the assumed configuration.

In the case of array **A**, the trigger logic will search for a coincidence in the defined GTU of $\geqslant n$ pixels per sector with pixel threshold $\geqslant m$ equivalent *pe*s whereas, for the **D** configuration, a coincidence of $\geqslant n$ pixels per sector is required to trigger an event. It is worthwhile underlining that, even though the trigger logic is based on the same principle, an evident difference exists between the two cases. In fact, system **A** uses simultaneously pixel position information (x_p, y_p) and its signal intensity while system **D** uses only the pixel position information due to the lack of information on pixel signal intensity resulting from the

[2] Actually, gain uniformity as reported by Hamamatsu and as measured in lab, is of the order of 1:3. For SPC, gain non-uniformity can be handled designing a front-end electronics capable to set discriminator trigger thresholds for each channel so to adjust, during the calibration phase, all the threshold levels at the lower pixel threshold observed. This is not so straightforward for charge integration.

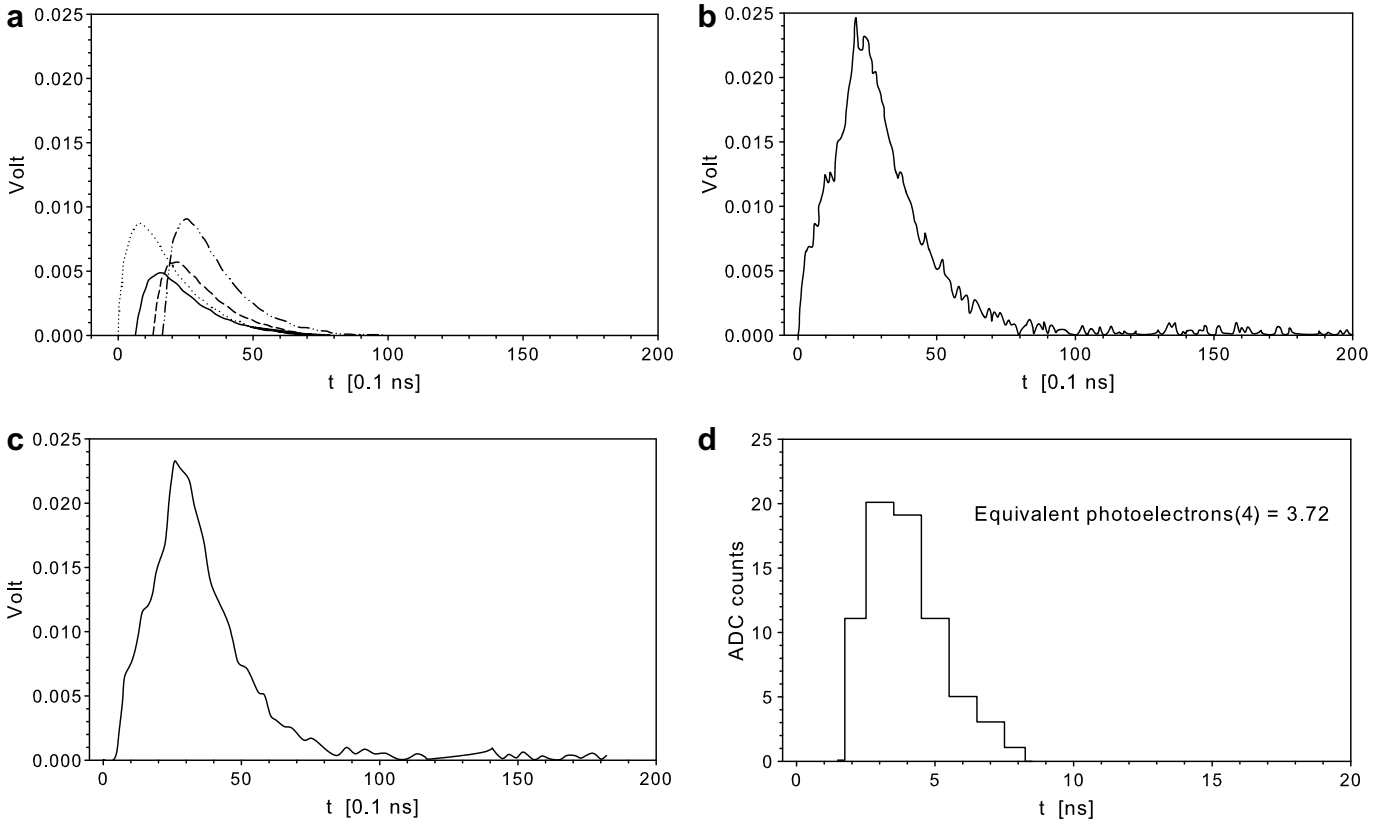

Fig. 4. The pixel signal simulation steps. (a) Single *pe*s belonging a pixel are individually converted to a voltage pulse according to Eq. 1 and noise factor (NF) variance and inverted. Individual *pe*s arrival times are taken by CORSIKA and fluctuated in agreement with the characteristic PMT transit spread time. (b) Pulses are summed. At this stage electronics noise is summed too. (c) The signal is cleaned from high frequency component by means of a filter. (d) Signal is sampled by a 1 GHz to 10 bit FADC. The sum of the sampled signal, converted in Volt, and divided by the *pe* equivalent value $\overline{V}_{pe}$ ($\overline{V}_{pe} \propto \overline{Q}_{pe}$) gives the number of equivalent *pe*s per pulse.

binary mode adoption (every pixel that will detect 1 *pe* or more will be always set to 1, otherwise to 0). Limiting the NSB "fake triggers" to a reasonable rate prevents overload of the data acquisition electronics and confined dead time to below a few percent. To define operational parameters of the trigger, the maximum tolerable rate has been determined for each telescope by a Monte Carlo study. The NSB simulations take into account the focal plane geometries and the specific size of the pixels. The mean *pe* probability per pixel per GTU is calculated as:

$$\mathrm{NSB}_{\mathrm{pixel}} = \langle \mathrm{NSB} \rangle \cdot A_{\mathrm{optics}} \cdot \Omega_{\mathrm{pixel}} \cdot \mathrm{GTU} \cdot \varepsilon_{\mathrm{tot}} \tag{3}$$

where $\langle \mathrm{NSB} \rangle = 2200$ photons $\mathrm{sr}^{-1}\,\mathrm{m}^{-2}\,\mathrm{ns}^{-1}$ (in the 300–600 nm wavelength band) is the averaged night sky background, $A_{\mathrm{optics}} = 3.5\,\mathrm{m}^2$ is the optics collecting area, $\Omega_{\mathrm{pixel}} = 1.6 \times 10^{-6}$ sr (**D**), $\Omega_{\mathrm{pixel}} = 6.4 \times 10^{-6}$ sr (**A**), GTU = 10 ns and $\varepsilon_{\mathrm{tot}} = 6.5\%$, the latter obtained by convolving optics, light guides and photomultiplier detection efficiencies (quantum efficiency plus collecting efficiencies). From the above formula, the resulting mean values of *pe*/pixel/10 ns due to the $\langle \mathrm{NSB} \rangle$ are 0.032 for configuration **A** and 0.008 for **D** configuration, respectively.

Random values drawn from a Poisson distribution with these mean values are used to distribute the number of resulting *pe*s uniformly on all the pixels of the whole focal plane, for each GTU.

For configuration **A**, the number of *pe*s in each pixel is converted into *pe* equivalent signal, following the procedure described in Section 3.2. For configuration **D**, each of the discriminated signals belonging to the pixels with one or more than 1 *pe* is set to 1 *pe* ("pixel-on") according with the binary mode operation. The pattern recognition algorithms, with the appropriate parameters, finally make a search for coincidences. A visualization of a snapshot of the focal plane pixels for both the configurations is shown in Fig. 5. The results for accidental coincidences are based on a statistics of 10 million simulated background events repeated for both configurations.

Fig. 6, top panel, shows the NSB single telescope accidental trigger rate as function of the pixel threshold for a required multiplicity of at least 3 pixels per sector; the pixel gain fluctuations (±6% around the mean value of σ_{pe}, as detailed in Appendix) are also shown. The simulations have been carried out by applying the average value of σ_{pe} corresponding to 0.43. Fig. 6, bottom panel, shows the NSB accidental trigger rate as function of the pixels multiplicity per sector.

According to these outcomes, the single telescope rate trigger has been set to 200 Hz for both the configurations,

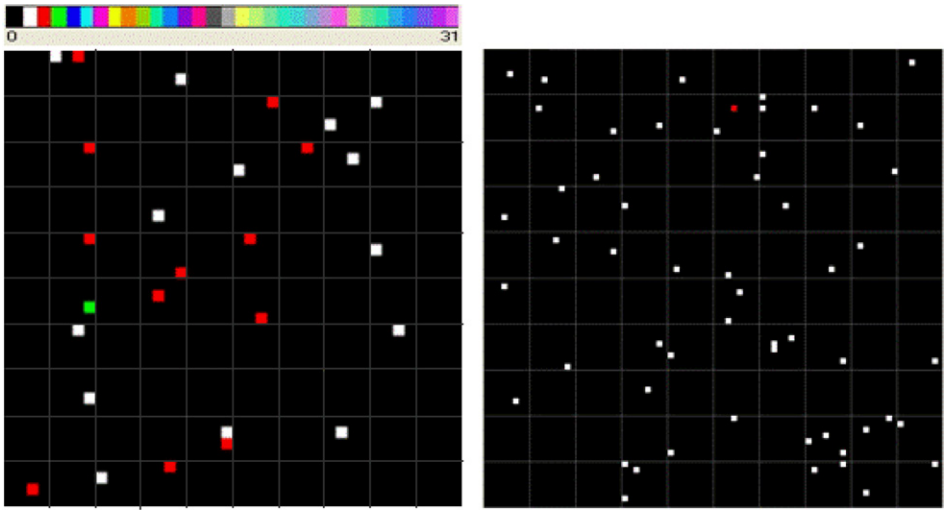

Fig. 5. Snapshots of the focal plane pixels for **A** (on the left) and **D** (on the right) configurations. Grids represent how the MAPMTs are mapped on the focal planes. The color bar (continuous for **A** and discrete for **D**) indicates the *pe* multiplicity. The red point (multiplicity 2) appearing on the right figure (**D** configuration) will be set to "1", before run the pattern recognition. Note the different size of pixels between **A** and **D** configurations. (For interpretation of the references to color in this figure legend, the reader is referred to the web version of this article.)

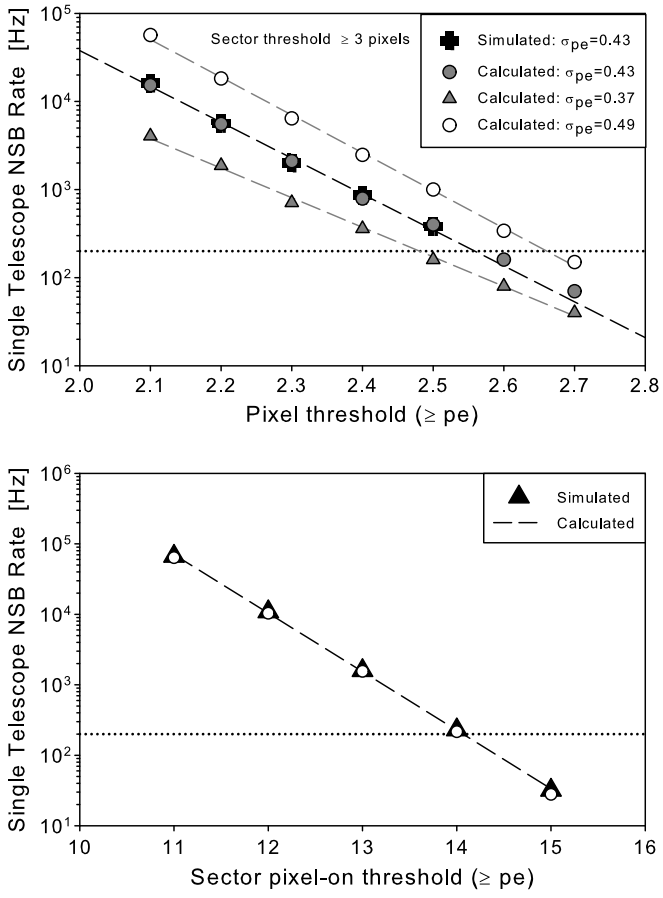

Fig. 6. The single telescope rate as a function of equivalent *pe*s threshold for a sector threshold $\geqslant 3$ pixels (top panel), and as a function of the sector pixel threshold (bottom panel). The horizontal dotted line indicates 200 Hz rate. The dashed regression lines are the values obtained by analytical calculation. Statistical error bars are smaller than the symbols size.

about a factor 2 of the expected hadron trigger rate. This means that a sector with at least 3 pixels, with threshold of 2.55 equivalent *pe*s (**A**) and a pixels-on threshold of 14 (**D**) will be required in order to have the same accidental rate due to NSB.

4. Results

In this section results are presented both for the case of one single telescope and for a 3-fold telescopes coincidence with the layout shown in Fig. 1. Trigger efficiencies are reported for both the cases and for configurations **D** and **A** using the threshold values estimated in Section 3.3. To check the quality of the trigger, triggered events has been reconstructed. Hillas parameters [1] have been evaluated and, as a representative figure for comparison, the value at 68% of the *Miss*[3] parameter distribution has been determined. A graphical representation of the involved steps in triggering and analyzing events is shown in Fig. 7 for the same triggered event on a telescope.

4.1. Single telescope

The CORSIKA simulated gamma-induced showers and the simulation chain described in Section 3.1 have been used to assess the single telescope trigger efficiency in configurations **A** and **D**. The obtained efficiency curves are shown in Fig. 8. Table 1 summarizes the efficiency ratio $R = D/A$ between the two configurations.

The percentage of reconstructed events with respect to the triggered events for each bin of energies related to the

[3] The *Miss* is defined as the perpendicular distance of the centre of the field (the source) from the major image axis.

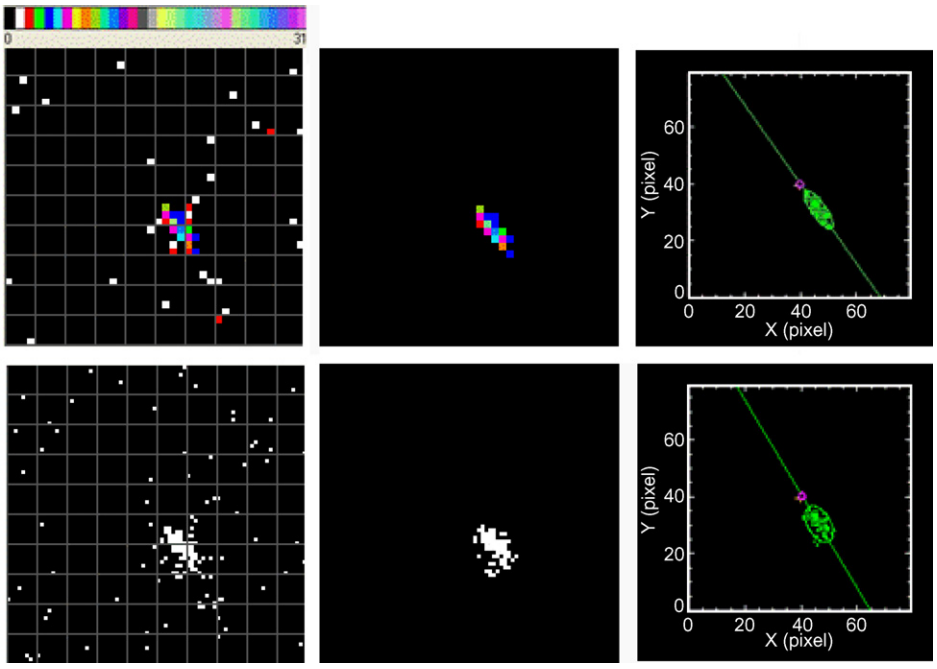

Fig. 7. Triggered gamma shower and reconstructed ellipses for **A** (top) and **D** (bottom) configuration respectively. The raw images are shown at the left. The regions of interest are selected by the pattern recognition algorithm (center). Hillas parameters are calculated fitting to ellipses the regions of interest (right). The image is treated as a binary image with all non-zero pixels considered as 1 for **D** configuration whereas a weighted transform, with the weighting given by the pixel intensity, is performed in case of **A** configuration.

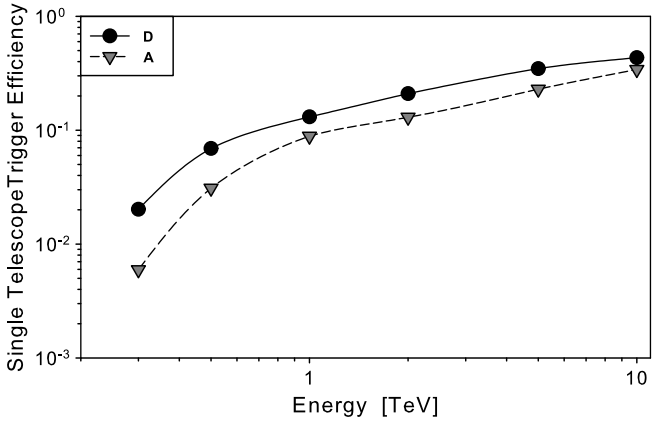

Fig. 8. Simulated trigger efficiencies for the **D** and **A** configurations. Statistical error bars are smaller than the symbols size.

Table 1
Single telescope – trigger ratio between **D** and **A** configurations vs. energy

Energy (TeV)	Single trigger ratio R_{single}
0.3	3.40 ± 0.06
0.5	2.23 ± 0.06
1	1.48 ± 0.03
2	1.61 ± 0.02
5	1.51 ± 0.02
10	1.27 ± 0.01

two configurations is reported in Table 2. Less than 1% of the events were rejected by the reconstruction algorithm applied to the two cases.

Table 2
Single telescope – percentage of reconstructed events vs. energy for the **D** and **A** configurations

Energy (TeV)	**D** (% reco)	**A** (% reco)
0.3	99.8	99.2
0.5	99.8	100.0
1	99.8	99.8
2	99.6	99.9
5	99.7	99.8
10	99.8	99.8

The 68% value of the *Miss* distribution is shown in Fig. 9 as a function of the energy.

The good agreement between the **D** and **A** curves indicates that no bias was introduced, within the intrinsic pixel resolution.

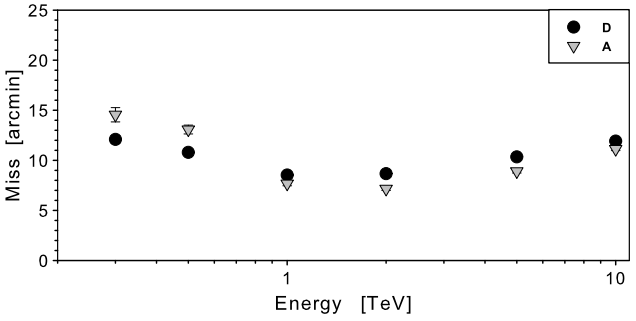

Fig. 9. The *Miss* parameter (value at 68%) for **D** and **A** configuration in case of one single telescope. At energy >0.5 TeV, the statistical error bars are smaller than the symbols size.

4.2. 3-fold Coincidence telescopes

In the case of the three telescopes in coincidence, the ratio of the trigger efficiencies substantially increases. This is what expected, due to the multiplicative contributions of single trigger efficiencies ($R_{3\text{-fold}} \propto R^3_{\text{single}}$). The obtained trend is shown in Fig. 10, where the trigger efficiency for configurations **D** and **A** is plotted as a function of the energy. Table 3 reports the ratio between **D** and **A** calculated at the various energies.

Table 4 gives the percentage of reconstructed events with respect to the triggered events for each bin of energies considered and for both the **D** and **A** configurations. On average, less than 1% of the triggered events were rejected by the reconstruction software for **D** and **A**, respectively.

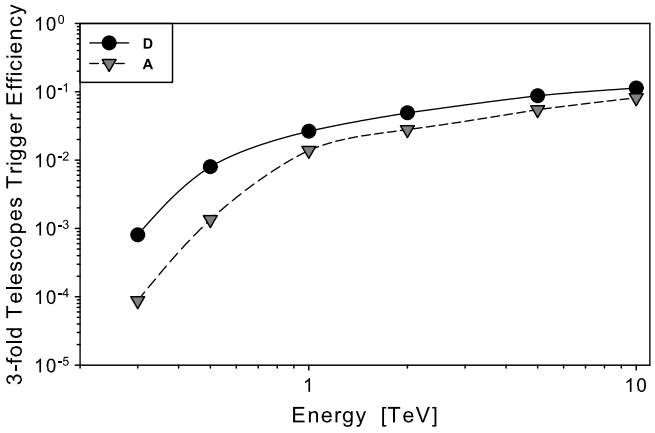

Fig. 10. 3-Fold Trigger efficiencies as a function of energy. Statistical error bars are smaller than the symbols size.

Table 3
3-folded Telescopes – trigger ratio between **D** and **A** configurations vs. energy

Energy (TeV)	3-fold Trigger ratio $R_{3\text{-fold}}$
0.3	9.16±1.27
0.5	5.92 ± 0.71
1	1.91 ± 0.08
2	1.76 ± 0.05
5	1.60 ± 0.04
10	1.39 ± 0.04

Table 4
3-fold Telescopes – percentage of reconstructed events vs. energy for the **D** and **A** configurations

Energy (TeV)	**D** (% reco)	**A** (% reco)
0.3	99.4	100.0
0.5	99.4	100.0
1	99.8	99.8
2	99.8	99.9
5	99.7	99.8
10	99.7	99.9

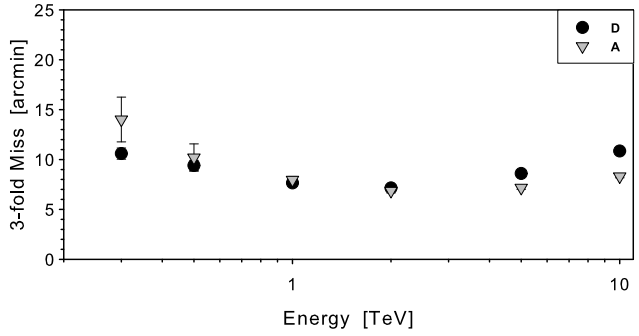

Fig. 11. Average values of the *Miss* parameter (68%) for **D** and **A** configurations.

Fig. 11 shows the average values calculated at 68% of the distribution of the *Miss* mean value obtained as arithmetic mean of the individual *Miss* values of each of the three images projected on the focal plane, as a function of energy in both the **D** and **A** cases. Once again, the small differences in the graph are within the intrinsic pixel resolution.

4.3. Energy reconstruction and photo-electrons pile-up

Although energy reconstruction and resolution are beyond the scope of this study (a specific paper will follow) it is important to refer to the *pe*s pile-up which could in principle limit the resolving power of the SPC technique. The effect could be relevant for the detection of Cherenkov light, where a bunch of photons, typically within few ns, is received in an area of less than 0.5 squared degrees, causing unavoidable *pe*s accumulation in the pixels.

It is clear that the pixel size is an important parameter for maintaining the linearity within the demanded dynamic range, as required by any experiment. An easy way to deal with this problem could be to diminish as much as possible the pixel size so to reduce the probability of pile-up, but this is not always viable due the physical dimension of light-sensors available on the market and to the consequent rise of read-out channels leading to an increasing in complexity and cost. A compromise is to keep the pixel dimension within what is available "off-the-shelf" on the market, and try to correct statistically for the system non-linearity. This, to a certain extent, can be applied as follows.

Let suppose, in first approximation, that N *pe*s are uniformly distributed onto an area S, and that this area S is divided in L equal parts. The average number of *pe*s in each part is: N/L and the probability to have 1 or more *pe*s is:

$$P(\geqslant 1) = 1 - e^{-N/L}$$

The total number of parts with 1 or more *pe*s is then:

$$M = L \cdot (1 - e^{-N/L})$$

that leads to:

$$N = -L \cdot \ln(1 - M/L)$$

Knowing L (parts) and the measured value M (number of *pe*s), the "true" value N can be estimated.

Since the area of the event-image on the focal plane changes depending on energy and distance of the shower core from the telescope itself, a variable area S has to be assumed, event by event. This area can be calculated as the ellipse area defined by the measured Length and Width of the shower image and subsequently, dividing it by the known pixel area, in order to obtain L.

A more accurate formula for the correction of non-linearity, that does not require *pe*s density to be uniform over the ellipse areas, can be obtained imposing signals (*pe*s) Gaussian distributed in two dimension over the ellipse-image area (Length and Width). Let be σ_{Width} and σ_{Length} the 68% of the measured Length and Width of the ellipse-image and $\Delta X = \Delta Y$ the detector pixel size; then:

$$G = k \cdot \mathrm{e}^{-\frac{1}{2}\left(\frac{\Delta X^2}{\sigma^2_{\text{Width}}}+\frac{\Delta Y^2}{\sigma^2_{\text{Length}}}\right)}$$

represents the trial distribution function with k as normalization factor. The equation for N can be therefore rewritten as:

$$N = -L \cdot \ln(1 - M \cdot G/L)$$

Fig. 12 shows the scatter plot of the measured and corrected number of *pe*s as a function of the actual number of *pe*s (from CORSIKA) and the histogram of the deviations between the actual counts and the corrected ones. This approach has been applied to a data set of gamma-induced showers of energy between 0.3 and 10 TeV with core scattered over an area of 800×800 m^2 and selecting events with numbers of *pe*s ranging from 14 to 1000 over the ellipse area.

Table 5 shows the standard deviation of the distributions obtained binning, in *pe*'s size, the overall data set with corresponding progressive bin values: 14–100, 101–200, etc.

Table 5
Standard deviation of the distributions [(simulated − reconstructed)/simulated]

Bin (*pe*'s size)	σ (%)
14–100	25.1 ± 0.3
101–200	19.9 ± 0.4
201–300	20.2 ± 0.6
301–400	18.2 ± 0.7
401–500	21.1 ± 1.1
501–600	23.8 ± 1.2
601–700	25.8 ± 1.5
701–800	28.9 ± 2.0
801–900	23.8 ± 2.2
901–1000	19.1 ± 2.1

4.4. Single telescope energy threshold and low energy telescope

Making use of the above results and of a further set of 220,000 gamma-induced showers simulated at an energy of 100 GeV, the expected energy threshold for each configuration can be calculated and compared.

Fig. 13 shows the differential rate for a Crab-like source (at 0° zenith angle) for configurations **D** and **A**, in the case of single telescope. The predicted rate is obtained multiplying the effective area by the assumed differential spectrum (power index = 2.49) at the simulated energies as marked in the plots. It is evident that configuration **D** exhibits a lower energy threshold with respect to the configuration **A**: 365 and 460 GeV at the curve peaks, respectively. This difference in energy threshold can be translated in terms of difference in optics collecting area by fixing the same energy threshold. If the total efficiency for both the systems is kept identical, then it is possible to estimate the equivalent optics area of the configuration **D** at the energy threshold of the configuration **A** and vice versa. This relation can be expressed as:

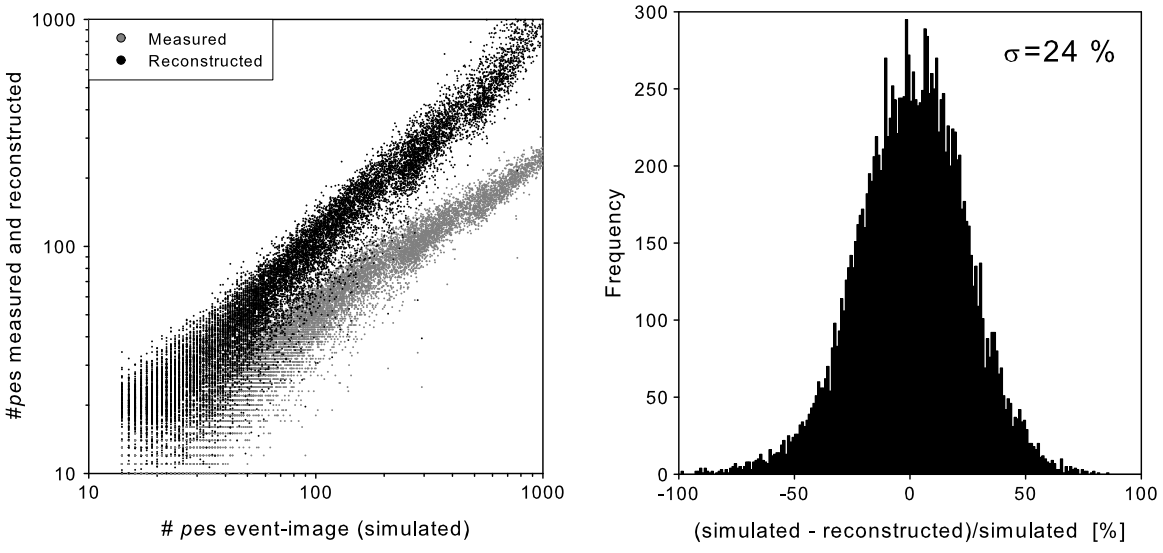

Fig. 12. Scatter plot of the measured and corrected number of *pe*s as a function of the actual number of *pe*s (left), and histogram of the deviations (right).

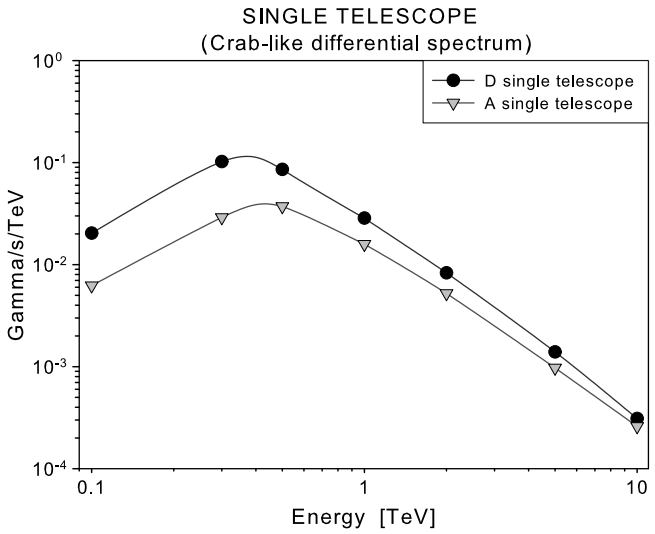

Fig. 13. Differential rate as a function of the energy for **D** and **A** configurations. Energy threshold is defined at the peak of the curve.

$$\sqrt{\frac{O_D}{O_A}} \approx \frac{E_{thr\,D}}{E_{thr\,A}} \tag{4}$$

with O_D the optics area of **D** system, O_A the optics area of **A** system, $E_{thr\,D}$ and $E_{thr\,A}$ the energy thresholds of **D** and **A** configurations respectively. Substituting in Eq. 4 the respective values of energy thresholds, a reduction of $\sim 37\%$ in the optics collecting area is achieved using the SPC method.

As a direct consequence of this result, a hypothetical low energy telescope (20–100 GeV) could be conceived. It should have, for an energy threshold of ~30 GeV, a mirror dish of 400 m^2, highly pixelizated camera with suitable front-end and trigger electronics. Fig. 14 shows the differential rate as a function of energy for a hypothetical telescope layout based on SPC method and design specifications defined in Table 6.

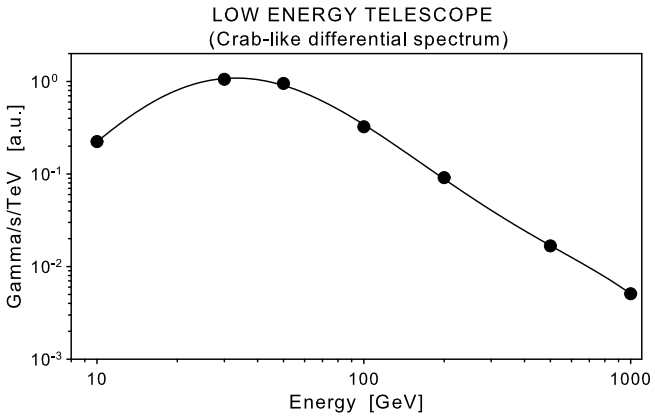

Fig. 14. Differential rate as a function of the energy for the Low Energy Telescope. The points onto the curve have been calculated by scaling.

Table 6
Low energy telescope – design specifications

Altitude (m)	2200
Optics total area (m^2)	400
F number	1.2
Total FoV (°)	3.2
Number of MAPMT	750
Type of MAPMT	Hamamatsu H9500 (16 × 16 pixels)
Pixel size	3.2 mm to 0.007°
MAPMT FoV (sr)	2.24×10^{-7}

5. Discussion and conclusions

The performance of similar telescope layouts using different approaches for the front-end electronics has been studied and compared at the level of the trigger efficiencies and energy thresholds. The results obtained adopting SPC for IAC instruments are remarkably encouraging. For a single telescope and at the lowest energy, the predicted enhancement of a factor greater than 3 with respect to the analog mode assures a considerable increase in effective area. The effect becomes more significant (a factor >9) in the case of the three-telescope coincidence.

A big effort has been put in the verification of the accuracy of simulation and analysis for both the techniques. Several tests and checks of the codes have been performed in order to guarantee unbiased estimators in the comparison of the two methods within, naturally, the statistical uncertainties. Pulse generation simulation and single electron response have been compared with actual experimental measurements. NSB has been evaluated using an "*ad hoc*" Monte Carlo code and results verified by comparison with analytical calculations and extrapolating actual experimental data. Possible incoherences in trigger selections have been ruled out analyzing the shower images making use of the Hillas parameters. Comparison of the representative *Miss* parameter for the two methods, both for single telescope and 3-fold coincidence, shows no evidence of any bias. Conversely, for the same energy threshold, configuration **D** allows a ~37% reduction in the optics collection area.

Summarizing, the benefits of a telescope design based on the SPC digital approach with respect to the analog one, are:

- lower energy threshold (with the same mirror area);
- smaller mirror area (for the same energy threshold);
- smaller telescope structure (for the same *f*-number);
- better pixel angular resolution due to smaller pixels;
- simpler front-end electronics;
- feasibility of using high-pixelization devices (for example, Hamamatsu H9500) avoiding light guides adapters.

While the drawbacks are:

- higher pixelization requiring a considerable number of channels to manage;
- needs of integrate the front-end electronics in a customized application specific integrated circuit (ASIC).

The SPC technique is certainly worth of further studies and experimental tests. A fundamental step for validating

this technique will be carried out by the GAW [15,16] collaboration. The first of the three planned GAW telescopes of 3.5 m^2 will be installed at Calar Alto (Spain) by the middle of 2008. The experimental measurements will allow to check the results of the simulation studies and, certainly, to learn more on this technique.

Appendix. Pulse simulation

The approach adopted in the present work consists of using the actual measured single electron response (SER) as an input to the Monte Carlo pulse simulation where photoemission combined statistics can be expressed as the relative variance in terms of single photon electron anode pulse height voltage V_H. Pulses from a PMT, in pure SER regime, have an amplitude variance proportional to the gain variance V_G that in turn can be expressed as

$$\frac{V_G}{\langle G\rangle^2} = \frac{V_Q}{\langle Q\rangle^2}$$

where the fractional variance $V_Q/\langle Q\rangle^2$ is deduced from the measured SER spectrum and $\langle G\rangle = \langle Q\rangle/e_c$ with e_c the elementary charge. The voltage pulse height distribution is obtained by varying the gain G in Eq. 1 as a Gaussian of mean 0 and variance $V_G\langle G\rangle^2$.

The pulse height distribution for number of photo-electrons greater than 1 is simulated using the superposition principle. The resulting pulse waveform, including electronics noise, is then amplified and inverted, filtered, and sampled with a 10 bit to 1 GHz FADC; a sketch of this procedure is shown in Fig. 15.

Operative parameters

The PMT operative parameters used for the pulse simulation are:

Gain: 1.58×10^6
$C_{eq.}$ (F): 10^{-12}
$R_{eq.}$ (Ω): 50
Pulse rise time (s): 1.5×10^{-9}
Dark current (A): 4×10^{-10}
Noise figure: 1.185
Transit time spread (ns): 0.6
FADC resolution (mV): 0.5
Amplifier: ×10 (320 MHz bandwidth)

Crosscheck with experimental data

In order to test and verify the pulse simulation software, a comparison with experimental result has been carried out. The MINOS collaboration [17] has reported on measurements of the gain efficiency, linearity, crosstalk and dark noise of 219 MAPMT R7600-00-M64. The accurate statistics performed on these PMTs shows several important features; among them, an average crosstalk of about 4%, a dark noise rate of 260 Hz per PMT and a pixel gain uniformity within 15–25%. Moreover, they have shown that, using single-electron spectra, the average RMS width of all the pixels was $43\% \pm 6\%$ of the peak position. These results have been confirmed, testing, in our lab, a reduced sample of 6 MAPMTs. The incidence of after-pulses has been also measured for the 6 PMTs. Less than 2% of after-pulses per pixel are created in the time window between 10 and 750 ns.

Digital mode

The comparison between measured and simulated pulses of the single photon counting trigger efficiency as a function of the discriminator threshold is shown in Fig. 16. The good performance of the measured trigger efficiency is due to the greatest care and skill in design the front-

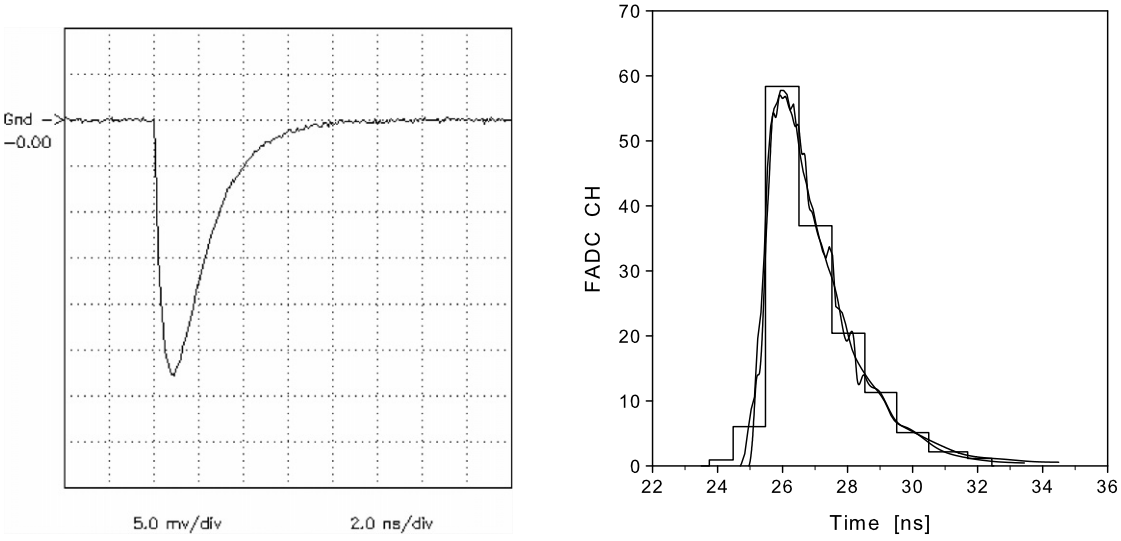

Fig. 15. The pulse simulation: pulse shape (left) and its digitalization (right).

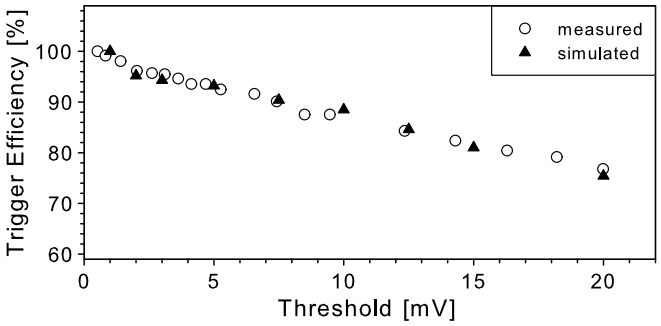

Fig. 16. SPC trigger efficiency vs. discriminator threshold for measured and simulated signal.

end electronics [18]. A value of 90% (10 mV) of trigger efficiency has been introduced in the computation of the total efficiency reported in Section 3.3.

Analog mode

The comparison of the average charge $\langle Q \rangle$ of SER measured spectra well agreed with the simulated ones within 5% for all considered spectra. Fig. 17 reports a measured pulse height spectrum in unit of mV · ns, using a LeCroy 4 GS/s oscilloscope. In the same figure, the simulated pulse height spectrum is superimposed to the measured one. In this case, the pulse simulation gain parameter has been set to $G = 10^6$ and the pulse distribution width to 0.43 of the peak position as determined by arithmetic computation of the measured SER.

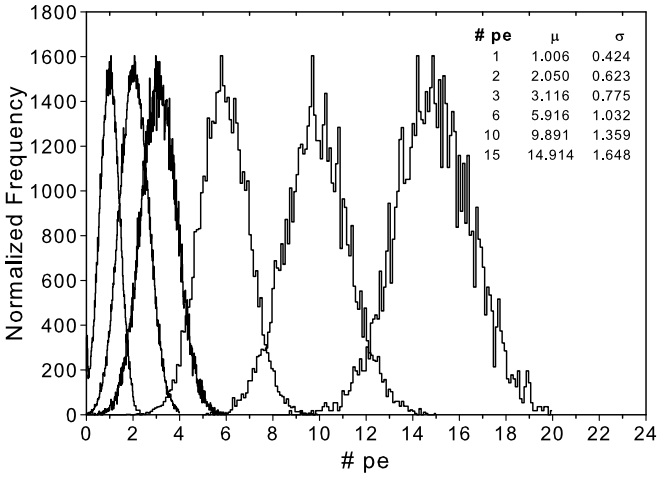

Fig. 18. The distribution of *pe*s as result of the pulse analog conversion.

Finally, from the simulated gamma data set, the response of the pulse simulation to multi-*pe*s pulses has been verified selecting, on the 40 × 40 pixels matrix, a sample of pixels exhibiting a multiplicity of 1, 2, 3, 6,10, 15 *pe*s. In correspondence of these pixels, the respective fractional values in *pe* unit has been extracted and recorded. The result of this analysis is shown, in graphical and numerical form, in Fig. 18. The means (μ) and the dispersions (σ) around the mean values of the multi-*pe*s distributions result consistent with the expected Gaussian distribution of standard deviation $\sqrt{(n)} \times \sigma_{pe}$ and mean n where n is the number of *pe*s and σ_{pe} is the single *pe* standard deviation set to 0.43.

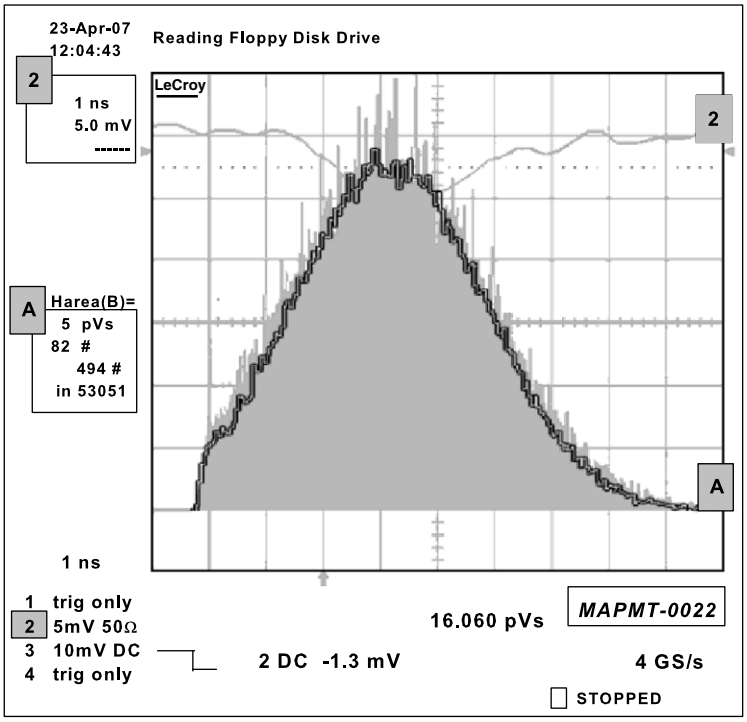

Fig. 17. Pulse height spectrum as seen at the oscilloscope; the simulated spectrum (bold line)is superimposed to the measured one.

References

[1] A.M. Hillas, Space Sci. Rev. 75 (1996) 17.
[2] M.F. Cawley, T.C. Weekes, Exp. Astron. 6 (1995) 7.
[3] T.C. Weekes et al., Astrophys. J. 342 (1989) 379.
[4] A. Daum et al., Astropart. Phys. 8 (1997) 1.
[5] H. Kubo et al., New Astron. Rev. 48 (2004) 323.
[6] T.C. Weekes et al., Astropart. Phys. 17 (2002) 221.
[7] E. Lorenz, MAGIC Collaboration, New Astron. Rev. 48 (2004) 339.
[8] J.A. Hinton, H.E.S.S. Collaboration, New Astron. Rev. 48 (2004) 331.
[9] W. Galbraith, J.V. Jelley, Nature 171 (1953) 349.
[10] Hamamatsu – Photomultiplier Tubes and Assemblies (for Scintillation Counting and High Energy Physics), 1998.
[11] D. Heck, J. Knapp, Extensive Air Shower Simulation with CORSIKA – A User's Guide, Version 6.203 from April 19, 2005.
[12] N.N. Kalmykov, S.S. Ostapchenko, A.I. Pavlov, Nucl. Phys. B (Proc. Suppl.) 52B (1997) 17.
[13] S.S. Ostapchenko, Nucl. Phys. B (Proc. Suppl.) 151 (2006) 143, 147.
[14] S. Castiglia, Qualificazione di un Fotomoltiplicatore MultiAnodo per Applicazioni di Monitoraggio Spaziale, Master Thesis, Dept. of Electronic Engineering, University of Palermo, 1999.
[15] G. Cusumano et al. (GAW Collaboration), in: Proc. 30th ICRC Conference, Merida, Mexico, 2007.
[16] M.C. Maccarone et al. (GAW Collaboration), in: Proc. 30th ICRC Conference, Merida, Mexico, 2007.
[17] N. Tagg et al., Nucl. Instrum. Methods Phys. Res. A 539 (2005) 668.
[18] P. Assis et al. (GAW Collaboration), in: Proc. 30th ICRC Conference, Merida, Mexico, 2007.